Letter | Editors' Suggestion

Ultrafast magnetostructural dynamics of MnAs

F. Vidal[1,*] Y. Zheng[1] E. Ferrari[2] E. Allaria[3] C. Spezzani,[3] C. Laulhé,[4] H. Popescu,[5] P. Atkinson,[1] N. Casaretto[1] M. Eddrief,[1] H. Wang,[6] J. Zhao,[6] M. Seaberg[7] R. Alonso-Mori[7] J. M. Glownia,[7] M. Chollet[7] H. Xu,[8] X. Huang,[8] F. Lima[8] D. Khakhulin,[8] I. J. Bermudez Macias[8] D. Vinci[8] M. Biednov,[8] Y. Jiang,[8] Y. Uemura,[8] F. Ardana-Lamas,[8] P. Zalden[8] C. Milne[8] and M. Sacchi[1,5]

[1]*Sorbonne Université, CNRS, Institut des NanoSciences de Paris, INSP, F-75005 Paris, France*
[2]*Deutsches Elektronen-Synchrotron DESY, Notkestrasse 85, D-22607 Hamburg, Germany*
[3]*Elettra-Sincrotrone Trieste, SS 14 km 163,5 in AREA Science Park, I-34149 Trieste, Italy*
[4]*Université Paris-Saclay, CNRS UMR8502, Laboratoire de Physique des Solides, F-91405 Orsay, France*
[5]*Synchrotron SOLEIL, L'Orme des Merisiers, Départementale 128, F-91190 Saint-Aubin, France*
[6]*State Key Laboratory of Superlattices and Microstructures, Institute of Semiconductors, Chinese Academy of Sciences, P.O. Box 912, Beijing 100083, People's Republic of China*
[7]*Linac Coherent Light Source (LCLS), SLAC National Accelerator Laboratory, Menlo Park, California 94025, USA*
[8]*European XFEL, Holzkoppel 4, D-22869 Schenefeld, Germany*

(Received 28 June 2024; accepted 13 September 2024; published 18 October 2024)

The ultrafast dynamics of α-MnAs magnetization and atomic structure are studied by the time-resolved magneto-optical Kerr effect and time-resolved x-ray diffraction after photoexcitation. In the basal plane of the hexagonal unit cell, Mn atomic disorder increases on a timescale of 400 fs, comparable to the laser-induced demagnetization timescale and significantly faster than As disorder (700 fs). This differentiation of the Mn and As relaxation times is observed in the ferromagnetic phase but disappears in the paramagnetic phase. These results strongly support recent density-functional theory calculations predicting that the magnetostructural phase transition of MnAs is driven by a change in nature of the dominant interactions between Mn 3*d* electrons, from magnetic exchange to bonding interactions.

DOI: 10.1103/PhysRevB.110.L140406

MnAs is a semimetal with properties such as giant magnetocaloric effect and colossal magnetoresistance, making it highly attractive for applications in magnetocalorics [1] and spintronics [2–6]. Epitaxially grown on GaAs(001), it forms a temperature-dependent self-organized pattern of alternating ferromagnetic (FM) and non-FM stripes, finding applications in magnetoacoustics [7,8] and in the control of an overlayer magnetization by either temperature or by a laser pulse [9]. The potential of MnAs for applications stems from its magnetostructural phase transitions. The low-temperature crystal structure [α phase, Figs. 1(a) and 1(b)] is hexagonal and ferromagnetic. At $T_c = 313$ K, a first-order phase transition to the orthorhombic structure occurs, with loss of FM order [β phase, Figs. 1(c) and 1(d)]. Above 400 K, the hexagonal structure is recovered in the paramagnetic γ phase.

Because of the dramatic structural and magnetic changes at the α-β transition, MnAs is a paradigmatic material for studying the strong coupling between lattice and magnetism. However, despite continuous modeling efforts [10–14], there is still no definite explanation for the unusual sequence of phase transitions in this compound. Density-functional theory (DFT) calculations by Łażewski *et al.* [15,16] involved a soft phonon, a vibration mode strongly coupled to the α-phase magnetization whose frequency vanishes near T_c, implying the displacement of both As and Mn atoms along the hexagonal-orthorhombic distortion path. The Mn magnetic moment reduction induces a softening of the mode, driving the structural transition towards the β phase.

Recent DFT calculations by Bocarsly *et al.* [17] are more specific and provide additional details about the driving force inducing the lattice instability. Their analysis suggests that the transition is driven by a distortion of the Mn sublattice resulting from the competition between exchange and bonding energy of the Mn $d_{x^2-y^2}$ orbitals in the hexagonal basal plane. In this framework, thermally induced magnetic fluctuations near T_c are sufficient to favor distortion within the hexagonal planes, with a large increase of the Mn structural disorder and stronger bonding of Mn d orbitals [Fig. 1(d)], the latter being hampered in the FM phase by the Pauli exclusion principle. This electronic scenario points to the reduction of the Mn magnetic moment as the phenomenon igniting the phase transition, which proceeds first via the displacement of Mn atoms.

In this Letter, we explore the subpicosecond magnetic and lattice dynamics of α-MnAs following the excitation by an optical laser pulse in order to test the transition mechanisms proposed in the literature. We use the time-resolved magneto-optical Kerr effect (MOKE) and x-ray diffraction (XRD) measurements to monitor the magnetization and structural dynamics, respectively. We find that ultrafast demagnetization occurs on a timescale of ∼300 fs and that the ultrafast

*Contact author: franck.vidal@sorbonne-universite.fr

 ©2024 American Physical Society

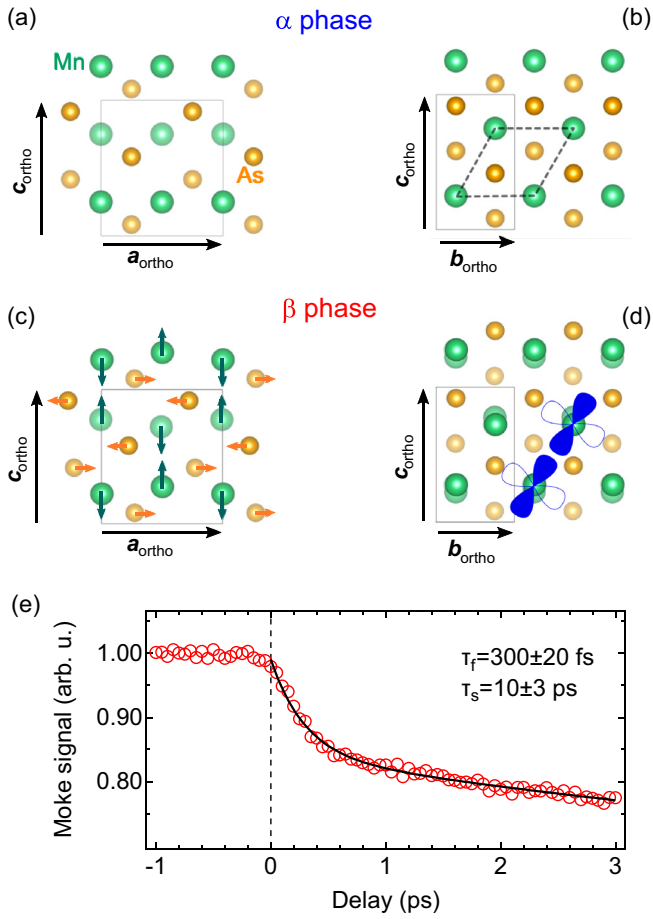

FIG. 1. Crystallographic structure in the (a), (b) α phase and (c), (d) β phase of MnAs. Arrows in (c) indicate the direction and sense of the atomic displacements involved in the hexagonal to orthorhombic transition. In (d) the Mn $d_{x^2-y^2}$ orbitals in the hexagonal planes are depicted in blue. The crystal structures were drawn with VESTA [18]. (e) Ultrafast demagnetization curve of MnAs/GaAs(001) at $T = 278$ K, pump fluence 1 mJ cm^{-2}. Symbol: experimental points; line: fit to Eq. (1).

dynamics of atomic disorder in α-MnAs is highly anisotropic and element dependent. In particular, our analysis reveals that Mn atomic disorder in the hexagonal planes evolves on a timescale of ~400 fs, significantly faster than that of As, and only slightly slower than the demagnetization timescale.

We used a 70-nm-thick MnAs epitaxial film grown by molecular beam epitaxy on GaAs(001) [19]. In this Letter, we use the orthorhombic system in order to describe each phase of MnAs with a common Bravais lattice. Moreover, this choice reflects better the symmetry of the system for MnAs/GaAs(001). The epitaxial relationship with $\mathbf{c}_{ortho} \parallel [001]_{GaAs}$ and $\mathbf{a}_{ortho} \parallel [1\bar{1}0]_{GaAs}$ was checked by laboratory x-ray diffraction measurements. Time-resolved magneto-optical measurements were performed using an amplified Ti:sapphire oscillator delivering pulses at 1 kHz with 100 fs duration. The sample was pumped at 780 nm with a fluence of 1 mJ cm^{-2} and probed using 390 nm pulses under the application of a static magnetic field. The temperature of the sample was set at 278 K during the measurements. Time-resolved x-ray diffraction measurements were performed at the XPP beamline of the Linac Coherent Light Source (LCLS) free-electron laser in Stanford [20] and at the FXE instrument of European XFEL [21], using the experimental geometry described in Ref. [22]. At XPP, the sample was excited by a pump laser pulse [800 nm wavelength, 43 fs duration full width at half maximum (FWHM), penetration depth 20 nm] and probed by 9.5 keV x-ray pulses (35 fs duration FWHM) at a 120 Hz repetition rate. The arrival time of each pulse was monitored by using the timing tool available at XPP [23], providing an overall time resolution of 55 fs. At FXE, we used similar pumping conditions (800 nm wavelength, 50 fs duration FWHM) and 9.3 keV x-ray pulses (with 1 eV bandwidth) for the probe. We used 8 pulses per train with 22 μs separation and 10 trains/s for an effective acquisition rate of 80 pulses per second [24]. The oscillation of coherent phonons in the β phase [22] at $T = 20\,^{\circ}$C were used to calibrate the fluence for comparison between the experiments performed at XPP and FXE. Time-resolved experiments were performed with the sample temperature kept at 282 ± 1 K for the ferromagnetic α phase and 404 ± 1 K for the paramagnetic γ phase.

Figure 1(e) shows a demagnetization curve of α-MnAs obtained at $T = 278$ K with a fluence of 1 mJ cm^{-2}. Two distinct timescales can be distinguished. At short delays, for $0 \leqslant \Delta t \leqslant 1$ ps, one can observe a sharp and fast drop of the magnetization. This initial demagnetization is followed by a slower decay for $\Delta t \geqslant 1$ ps. We attribute this change of behavior to the progressive heating of the sample at larger delays while the evolution at smaller delays is attributed to ultrafast demagnetization of the α phase without change in crystal symmetry. The data were fitted assuming two exponential decay processes for the intensity, with different time constants and amplitudes:

$$\frac{I(\Delta t)}{I_0} = 1 - a_f \exp(-\Delta t/\tau_f) - a_s \exp(-\Delta t/\tau_s). \qquad (1)$$

The initial laser-induced demagnetization is found to proceed with a characteristic time $\tau_f = 300 \pm 20$ fs.

Figure 2 presents a series of measurements performed on the 006 Bragg reflection, for various pump-probe delays Δt. As shown by the ω-Δt map of the diffracted intensity in Fig. 2(a), with ω being the incidence angle and Δt the pump-probe delay, we observe a single diffraction peak, corresponding to α-MnAs, up to 2.5 ps. Beyond this delay, the formation of a side peak at lower angle is observed and the main peak moves towards higher angles. Such behavior corresponds to the formation of a strain wave within the MnAs thin film and will not be discussed further here. The ω scans at fixed Δt can be fitted by using Lorentzian profiles, as shown in Fig. 2(b). Results of the fits for the peak position and width are given in Figs. 2(c) and 2(d). For $\Delta t \leqslant 1.5$ ps, the change in the angular position of the α 006 reflection is negligible. The width of the peak does not evolve significantly in the first ps after excitation, as shown in Fig. 2(d). Thus, the peak shift and broadening have minimal or no impact on the drop of the intensity which is the main change observed in the first ps following laser excitation. In the following we will thus concentrate on the variation of the intensity recorded at several Bragg peak positions, as determined at negative pump-probe delays.

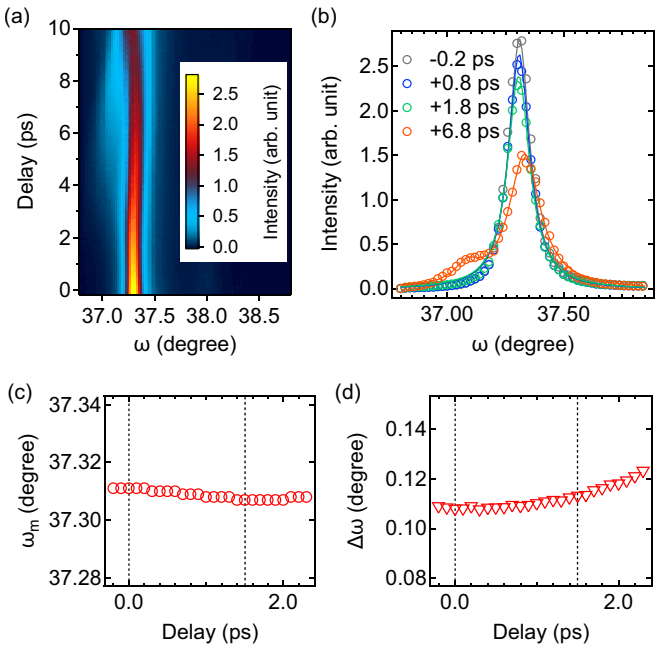

FIG. 2. Time-resolved diffraction measurements of the 006 Bragg reflection. (a) Map of the diffracted intensity as a function of the incidence angle ω and of the delay Δt. (b) Profiles at selected delays. Circles: data; lines: fits using Lorentzian profiles. (c) Fitted peak position and (d) peak width as a function of Δt. Pump fluence 5 mJ cm^{-2}.

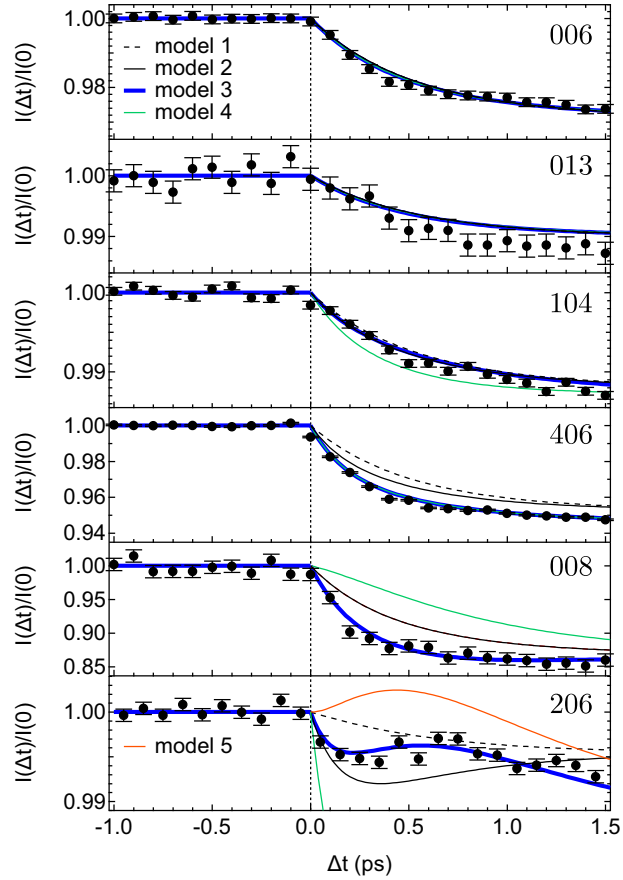

FIG. 3. Symbols: Time-resolved diffraction measurements of the 006, 013, 104, 406, 008, 206 Bragg reflections of ferromagnetic α-MnAs at $T = 282$ K, pump fluence of 1.5 mJ cm^{-2}. Lines: Model calculations based on Eqs. (2)–(7). Model 1: All time constants set to 550 fs. Model 2: $\tau_{11}^{\mathrm{As}} = 160$ fs, the others are set to 550 fs. Model 3: $\tau_{11}^{\mathrm{Mn}} = 700$ fs, $\tau_{11}^{\mathrm{As}} = 160$ fs, $\tau_{22}^{\mathrm{Mn}} = \tau_{33}^{\mathrm{Mn}} = 400$ fs, $\tau_{22}^{\mathrm{As}} = \tau_{33}^{\mathrm{As}} = 700$ fs. Model 4: $\tau_{11}^{\mathrm{Mn}} = 700$ fs, $\tau_{11}^{\mathrm{As}} = 160$ fs, $\tau_{22}^{\mathrm{Mn}} = \tau_{33}^{\mathrm{Mn}} = 700$ fs, $\tau_{22}^{\mathrm{As}} = \tau_{33}^{\mathrm{As}} = 400$ fs. Model 5 (for 206 reflection only): Variation on model 3, with $\tau_{11}^{\mathrm{Mn}} = 160$ fs. Models 1–4 are represented for each reflection (they superimpose for 006 and 013).

In order to track a possible anisotropy and/or element dependence of the structural dynamics, time-resolved XRD measurements were performed on the following Bragg reflections: 006, 406, 013, 104, 008, and 206. For 006, 406, and 013 reflections, the structure factor F_{hkl} can be written as

$$F_{hkl} = 4f_{\mathrm{Mn}}e^{-W_{\mathrm{Mn}}^{hkl}} + 4f_{\mathrm{As}}e^{-W_{\mathrm{As}}^{hkl}}. \quad (2)$$

In this equation, f_{As} and f_{Mn} are the atomic form factors and W_{Mn}^{hkl} and W_{As}^{hkl} are the Debye-Waller factors, given by

$$W_X^{hkl} = 2\pi^2\left[h^2(a^\star)^2U_{11}^X + k^2(b^\star)^2U_{22}^X + l^2(c^\star)^2U_{33}^X\right], \quad (3)$$

where U_{ii} are mean-square atomic displacements and X represents either Mn or As. For the 104 reflection, we have

$$F_{104} = -2\sqrt{3}f_{\mathrm{As}}e^{-W_{\mathrm{As}}^{104}}. \quad (4)$$

Thus, the 104 reflection is sensitive to the As atomic positions only. The 008 and 206 reflections were chosen because of out-of-phase contributions of Mn and As:

$$F_{008} = 4f_{\mathrm{Mn}}e^{-W_{\mathrm{Mn}}^{008}} - 2f_{\mathrm{As}}e^{-W_{\mathrm{As}}^{008}}, \quad (5)$$

$$F_{206} = 4f_{\mathrm{Mn}}e^{-W_{\mathrm{Mn}}^{206}} - 4f_{\mathrm{As}}e^{-W_{\mathrm{As}}^{206}}. \quad (6)$$

Figure 3 shows the normalized intensity of these Bragg reflections as a function of the pump-probe delay obtained at $T = 282$ K for the ferromagnetic α phase of MnAs. We observe that each reflection exhibits a distinct time constant for the initial intensity decay. This rules out any excitation of overdamped coherent oscillations in the system. Hence, the observed variations can only be accounted for by an ultrafast change in the Debye-Waller factors reflecting the incoherent excitation of phonons. Here, time-resolved diffraction allows us to track the evolution of the structural disorder in MnAs during ultrafast demagnetization.

In order to account for the distinct dynamics of these reflections, the data were modeled taking into account the finite pump penetration depth and assuming the following Δt-dependent evolution of the mean-square atomic displacements:

$$U_{ii}^X(\Delta t) = U_{ii}^X(0) + \Delta U_{ii}^X\left[1 - \exp\left(-\Delta t/\tau_{ii}^X\right)\right]. \quad (7)$$

Static bulk values of $U_{ii}^X(0)$ measured by x-ray diffraction can be found in the literature [25,26], but they can differ from those pertinent to MnAs/GaAs(001) epitaxial films, whose determination is not possible with a limited set of Bragg reflections. We have therefore adopted the following procedure, in order to limit the number of parameters in our analysis: We fix the $U_{ii}^X(0)$ values in the hexagonal plane ($i = 2$ and $i = 3$) to 0.017 Å^2, corresponding to the bulk value for Mn, and we adjust $U_{11}^X(0)$ to 0.024 Å^2 in order to match the ratio

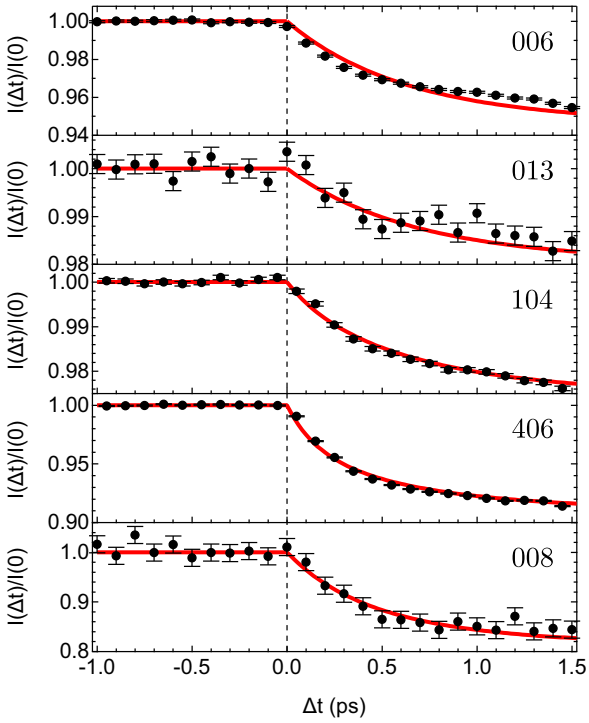

FIG. 4. Symbols: Time-resolved diffraction measurements of the 006, 013, 104, 406, 008 Bragg reflections of paramagnetic MnAs at $T = 404$ K, pump fluence of 1.5 mJ cm^{-2}. Lines: Model calculations with $\tau_{11}^{\mathrm{As}} = 160$ fs, the others τ_{ii}^{X} are set at 700 fs.

of intensities of the 006 and 406 reflections experimentally observed in MnAs/GaAs(001) [27].

The results of different approaches to modeling the experimental data based on Eqs. (2)–(7) are summarized in Fig. 3. Model 1, assuming a single value for all τ_{ii}^{X} time constants, results in a poor agreement for 206 and 406 reflections and was discarded. Including a fast component along $\mathbf{a}_{\mathrm{ortho}}$ slightly improves the match for 206 and 406 reflections (model 2), but worsens it significantly for the 008 reflection, which is very sensitive to the difference between τ_{33}^{As} and τ_{33}^{Mn}. In order to reproduce the full set of data, it was necessary to introduce three distinct time constants: $\tau_{11}^{\mathrm{Mn}} = 0.7$ ps, $\tau_{11}^{\mathrm{As}} = 160$ fs, $\tau_{22}^{\mathrm{Mn}} = \tau_{33}^{\mathrm{Mn}} = 400$ fs, $\tau_{22}^{\mathrm{As}} = \tau_{33}^{\mathrm{As}} = 700$ fs (model 3). We tested other models (4 and 5) in order to check the hierarchy of timescales. If one considers a fast timescale for As and a slow timescale for Mn in hexagonal planes, no agreement can be found for the 104 and 008 reflections (model 4). Starting from model 3 and considering a fast variation of U_{11}^{Mn} leads to an initial increase of $I_{206}(\Delta t)$ (model 5) in contradiction with the experiment. In conclusion, model 3 provides the best agreement with the experimental data. Using this model, the optimization of the ΔU_{ii}^{X} parameters shows that, in the hexagonal planes, the magnitude of the induced disorder is larger for Mn $[\Delta U_{22}^{\mathrm{Mn}}/U_{22}^{\mathrm{Mn}}(0) = \Delta U_{33}^{\mathrm{Mn}}/U_{33}^{\mathrm{Mn}}(0) = 0.25]$ than for As $[\Delta U_{22}^{\mathrm{As}}/U_{22}^{\mathrm{As}}(0) = \Delta U_{33}^{\mathrm{As}}/U_{33}^{\mathrm{As}}(0) = 0.155]$.

Figure 4 shows the normalized intensity of the 006, 406, 013, 104, and 008 Bragg reflections as a function of the pump-probe delay obtained at $T = 404$ K in the paramagnetic state. In sharp contrast to the behavior observed for the ferromagnetic state, the data can be modeled using a single time constant of 700 fs for all τ_{ii}^{X} except for $\tau_{11}^{\mathrm{As}} = 160$ fs. Thus, in the absence of ferromagnetic order, the Mn and As disorders evolve with the same time constant in the hexagonal planes.

The value of τ_{11}^{As}, common to both ferromagnetic and paramagnetic phases, indicates a channel of fast relaxation of the electronic energy to the lattice via incoherent excitation of phonons with displacements of As atoms along the hexagonal axis. This points towards a strong coupling with the B_{2g} mode [28], involving only movements of As atoms along $\mathbf{a}_{\mathrm{ortho}}$, in the early stages of the electronic relaxation. The need to consider phonon branches independently to explain the photoinduced dynamics has been highlighted previously in the case of simple metals [29] and polar semiconductors [30]. Ultrafast energy transfer to the optical modes in the early stages of the relaxation was observed previously in graphite [31], giving rise to the same kind of dynamics as observed here for the 406 reflection with two distinct time constants.

Comparison of the results obtained in the ferromagnetic and paramagnetic phases reveals similar structural dynamics except for in-plane Mn atoms. The fast variation of U_{22}^{Mn} and U_{33}^{Mn} occurs only in the presence of ferromagnetic order. Mn disorder in hexagonal planes increases with a time constant of 400 fs, which differs only slightly from the demagnetization time constant (300 fs).

In their DFT study, Łażewski *et al.* predict a strong dependence on the magnetization m of the frequency ν of the soft-mode implied in the phase transitions, with $\nu = -|\nu_0| + \lambda m^2$ [15]. The λ parameter that describes the spin-phonon coupling has a large value and complete softening is obtained for an 8% reduction of the magnetization. Such reduction of the magnetization is reached in the early stage of the laser-induced demagnetization, at $\Delta t \simeq 180$ fs. The complete softening of the mode, leading to a flat potential, would lead to an inertial dynamics with mean-square atomic displacements varying as Δt^2 [32]. This is not observed in our experiment. Thus, our measurements are not consistent with an ultrafast complete softening of the mode exhibiting a strong spin-phonon coupling.

In contrast, our results are compatible and agree with the model proposed by Bocarsly *et al.* [17] and can be interpreted as follows: Magnetic fluctuations, occurring during the demagnetization process, trigger a softening of the Mn sublattice in hexagonal planes. Spin flips make bonding of d orbitals possible in the hexagonal planes [see Fig. 1(d)]. This occurs before any changes in lattice symmetry and strain, which take place on a slower timescale. From the value of $\Delta U_{22}^{\mathrm{Mn}} = \Delta U_{33}^{\mathrm{Mn}}$, the mean-square displacement of Mn atoms reaches 0.021 Å^2, close to the maximum value observed at the α-β transition [25]. Overall, these results provide a microscopic description of the magnetostructural coupling in MnAs and strong experimental evidence in favor of the mechanism involving bonding of the Mn orbitals in the hexagonal planes proposed in Ref. [17].

In conclusion, our time-resolved study highlights the key ingredients of the magnetostructural coupling in α-MnAs. The ability to follow the structural dynamics in an element-specific manner by x-ray diffraction proved decisive in demonstrating the softening of the Mn sublattice. We believe that such

an approach, exploiting particular Bragg reflections or using resonant diffraction, could be generalized to the study of correlations in real time in other materials of fundamental and applied interest.

Use of the Linac Coherent Light Source (LCLS), SLAC National Accelerator Laboratory, is supported by the U.S. Department of Energy, Office of Science, Office of Basic Energy Sciences under Contract No. DE-AC02-76SF00515. We acknowledge European XFEL in Schenefeld, Germany, for provision of x-ray free-electron laser beamtime at FXE and would like to thank the staff for their assistance. We acknowledge support from CNRS through the PEPS-SASLELX program.

[1] D. H. Mosca, F. Vidal, and V. H. Etgens, Strain engineering of the magnetocaloric effect in MnAs epilayers, Phys. Rev. Lett. **101**, 125503 (2008).

[2] S. Sugahara and M. Tanaka, Tunneling magnetoresistance in fully epitaxial MnAs/AlAs/MnAs ferromagnetic tunnel junctions grown on vicinal GaAs(111)B substrates, Appl. Phys. Lett. **80**, 1969 (2002).

[3] M. Ramsteiner, H. Y. Hao, A. Kawaharazuka, H. J. Zhu, M. Kastner, R. Hey, L. Däweritz, H. T. Grahn, and K. H. Ploog, Electrical spin injection from ferromagnetic MnAs metal layers into GaAs, Phys. Rev. B **66**, 081304(R) (2002).

[4] V. Garcia, H. Jaffrès, J.-M. George, M. Marangolo, M. Eddrief, and V. H. Etgens, Spectroscopic measurement of spin-dependent resonant tunneling through a 3D disorder: The case of MnAs/GaAs/MnAs junctions Phys. Rev. Lett. **97**, 246802 (2006).

[5] P. N. Hai, S. Ohya, M. Tanaka, S. E. Barnes, and S. Maekawa, Electromotive force and huge magnetoresistance in magnetic tunnel junctions, Nature (London) **458**, 489 (2009).

[6] M. E. Nowakowski, G. D. Fuchs, S. Mack, N. Samarth, and D. D. Awschalom, Spin control of drifting electrons using local nuclear polarization in ferromagnet-semiconductor heterostructures, Phys. Rev. Lett. **105**, 137206 (2010).

[7] J.-Y. Duquesne, J.-Y. Prieur, J. A. Canalejo, V. H. Etgens, M. Eddrief, A. L. Ferreira, and M. Marangolo, Ultrasonic triggering of giant magnetocaloric effect in MnAs thin films, Phys. Rev. B **86**, 035207 (2012).

[8] P. Delsing, A. N. Cleland, M. J. A. Schuetz, J. Knörzer, G. Giedke, J. I. Cirac, K. Srinivasan, M. Wu, K. Coimbatore Balram *et al.*, The 2019 surface acoustic waves roadmap, J. Phys. D: Appl. Phys. **52**, 353001 (2019).

[9] C. Spezzani, E. Ferrari, E. Allaria, F. Vidal, A. Ciavardini, R. Delaunay, F. Capotondi, E. Pedersoli, M. Coreno, C. Svetina *et al.*, Magnetization and microstructure dynamics in Fe/MnAs/GaAs(001): Fe magnetization reversal by a femtosecond laser pulse, Phys. Rev. Lett. **113**, 247202 (2014).

[10] C. Kittel, Model of exchange-inversion magnetization, Phys. Rev. **120**, 335 (1960).

[11] C. P. Bean and D. S. Rodbell, Magnetic disorder as a first-order phase transformation, Phys. Rev. **126**, 104 (1962).

[12] N. Menyuk, J. A. Kafalas, K. Dwight, and J. B. Goodenough, Effects of pressure on the magnetic properties of MnAs, Phys. Rev. **177**, 942 (1969).

[13] L. Pytlik and A. Zieba, Magnetic phase diagram of MnAs, J. Magn. Magn. Mater. **51**, 199 (1985).

[14] I. Rungger and S. Sanvito, *Ab initio* study of the magnetostructural properties of MnAs, Phys. Rev. B **74**, 024429 (2006).

[15] J. Łażewski, P. Piekarz, J. Toboła, B. Wiendlocha, P. T. Jochym, M. Sternik, and K. Parlinski, Phonon mechanism of the magnetostructural phase transition in MnAs, Phys. Rev. Lett. **104**, 147205 (2010).

[16] J. Łażewski, P. Piekarz, and K. Parlinski, Mechanism of the phase transitions in MnAs, Phys. Rev. B **83**, 054108 (2011).

[17] J. D. Bocarsly, M. D. Johannes, S. D. Wilson, and R. Seshadri, Magnetostructural coupling from competing magnetic and chemical bonding effects, Phys. Rev. Res. **2**, 042048(R) (2020).

[18] K. Momma and F. Izumi, VESTA 3 for three-dimensional visualization of crystal, volumetric and morphology data, J. Appl. Crystallogr. **44**, 1272 (2011).

[19] L. Lounis, M. Eddrief, M. Sacchi, and F. Vidal, Layer-sensitive magneto-optical Kerr effect study of magnetization reversal in Fe/MnAs/GaAs(001), Appl. Phys. Lett. **111**, 232403 (2017).

[20] M. Chollet, R. Alonso-Mori, M. Cammarata, D. Damiani, J. Defever, J. T. Delor, Y. Feng, J. M. Glownia, J. B. Langton, S. Nelson *et al.*, The x-ray pump–probe instrument at the linac coherent light source, J. Synchrotron Radiat. **22**, 503 (2015).

[21] A. Galler, W. Gawelda, M. Biednov, C. Bomer, A. Britz, S. Brockhauser, T.-K. Choi, M. Diez, P. Frankenberger, M. French *et al.*, Scientific instrument Femtosecond X-ray Experiments (FXE): Instrumentation and baseline experimental capabilities, J. Synchrotron Radiat. **26**, 1432 (2019).

[22] F. Vidal, Y. Zheng, L. Lounis, L. Coelho, C. Laulhe, C. Spezzani, A. Ciavardini, H. Popescu, E. Ferrari, E. Allaria, J. Ma, H. Wang, J. Zhao, M. Chollet, M. Seaberg, R. Alonso-Mori, J. M. Glownia, M. Eddrief, and M. Sacchi, Ultrafast structural dynamics along the β-γ phase transition path in MnAs, Phys. Rev. Lett. **122**, 145702 (2019).

[23] M. Harmand, R. Coffee, M. R. Bionta, M. Chollet, D. French, D. Zhu, D. M. Fritz, H. T. Lemke, N. Medvedev, B. Ziaja, S. Toleikis, and M. Cammarata, Achieving few-femtosecond time-sorting at hard x-ray free-electron lasers, Nat. Photonics **7**, 215 (2013).

[24] W. Decking, S. Abeghyan, P. Abramian, A. Abramsky, A. Aguirre, C. Albrecht, P. Alou, M. Altarelli, P. Altmann, K. Amyan *et al.*, A MHz-repetition-rate hard x-ray free-electron laser driven by a superconducting linear accelerator, Nat. Photonics **14**, 391 (2020).

[25] V. Petkov, A. Zafar, D. R. Tadisetti, and M. A. M. Abeykoon, Lattice instability and magnetic phase transitions in strongly correlated MnAs, J. Phys.: Condens. Matter **35**, 315401 (2023).

[26] N. D. Zhigadlo, High-pressure growth and characterization of bulk MnAs single crystals, J. Cryst. Growth **480**, 148 (2017).

[27] L. Lounis, Propriétés magnétiques et structurales de Fe/MnAs/GaAs(001) et dynamique photo-induite des transitions de phase dans MnAs/GaAs(001), Ph.D. thesis, Université PSL, 2017.

[28] H. D. Lutz, H. Hauseler, and P. Willich, Gitterschwingungsspektren. XIV. NiAs- und Fe_3Se_4-Struktur, Z. Naturforsch. **30**, 308 (1975).

[29] L. Waldecker, R. Bertoni, and R. Ernstorfer, Electron-phonon coupling and energy flow in a simple metal beyond the two-temperature approximation, Phys. Rev. X **6**, 021003 (2016).

[30] D. K. Ferry, Non-equilibrium longitudinal optical phonons and their lifetimes, Appl. Phys. Rev. **8**, 021324 (2021).

[31] R. P. Chatelain, V. R. Morrison, B. L. M. Klarenaar, and B. J. Siwick, Coherent and incoherent electron-phonon coupling in graphite observed with radio-frequency compressed ultrafast electron diffraction, Phys. Rev. Lett. **113**, 235502 (2014).

[32] A. M. Lindenberg, J. Larsson, K. Sokolowski-Tinten, K. J. Gaffney, C. Blome, O. Synnergren, J. Sheppard, C. Caleman, A. G. MacPhee, D. Weinstein *et al.*, Atomic-scale visualization of inertial dynamics, Science **308**, 392 (2005).